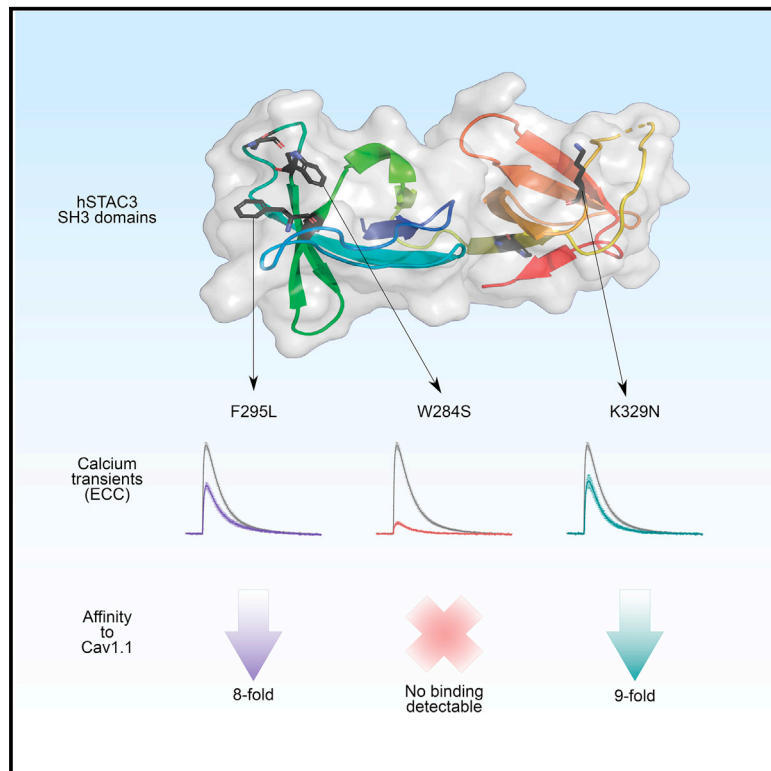


Structure

Multiple Sequence Variants in STAC3 Affect Interactions with $Ca_v1.1$ and Excitation-Contraction Coupling

Graphical Abstract



Authors

Britany Rufenach, Darren Christy, Bernhard E. Flucher, Jennifer M. Bui, Jörg Gsponer, Marta Campiglio, Filip Van Petegem

Correspondence

marta.campiglio@i-med.ac.at (M.C.),
filip.vanpetegem@gmail.com (F.V.P.)

In Brief

Combining X-ray crystallography, protein-interaction studies, EC-coupling assays, and molecular dynamics simulations, Rufenach et al. study the effects of STAC3 variants on structure and function. Several variants cause myopathy by disturbing the interaction with $Ca_v1.1$. They report a high-resolution structure of the human STAC3 tandem SH3 domains.

Highlights

- Multiple variants reduce binding affinity to $Ca_v1.1$ and calcium transients
- STAC3 tandem SH3 domains each consist of five-stranded antiparallel beta sheets
- Both STAC3 SH3 domains are important for interaction with Cav1.1
- MD simulations highlight similarities between STAC2 and STAC3 binding $Ca_v1.1$



Article

Multiple Sequence Variants in STAC3 Affect Interactions with Ca_v1.1 and Excitation-Contraction Coupling

Britany Rufenach,¹ Darren Christy,¹ Bernhard E. Flucher,² Jennifer M. Bui,¹ Jörg Gsponer,¹ Marta Campiglio,^{2,*} and Filip Van Petegem^{1,3,*}

¹Department of Biochemistry and Molecular Biology, University of British Columbia, Vancouver, BC V6T 1Z3, Canada

²Department of Physiology and Medical Physics, Medical University of Innsbruck, 6020 Innsbruck, Austria

³Lead Contact

*Correspondence: marta.campiglio@i-med.ac.at (M.C.), filip.vanpetegem@gmail.com (F.V.P.)

<https://doi.org/10.1016/j.str.2020.05.005>

SUMMARY

STAC3 is a soluble protein essential for skeletal muscle excitation-contraction (EC) coupling. Through its tandem SH3 domains, it interacts with the cytosolic II-III loop of the skeletal muscle voltage-gated calcium channel. STAC3 is the target for a mutation (W284S) that causes Native American myopathy, but multiple other sequence variants have been reported. Here, we report a crystal structure of the human STAC3 tandem SH3 domains. We analyzed the effect of five disease-associated variants, spread over both SH3 domains, on their ability to bind to the Ca_v1.1 II-III loop and on muscle EC coupling. In addition to W284S, we find the F295L and K329N variants to affect both binding and EC coupling. The ability of the K329N variant, located in the second SH3 domain, to affect the interaction highlights the importance of both SH3 domains in association with Ca_v1.1. Our results suggest that multiple STAC3 variants may cause myopathy.

INTRODUCTION

Excitation-contraction (EC) coupling is the process whereby an electrical signal on the plasma membrane of a muscle cell ultimately leads to muscle contraction. In skeletal muscle, this process relies on a mechanical link between the L-type voltage-gated calcium channel (Ca_v1.1) on the plasma membrane and the type-1 ryanodine receptor (RyR1) on the sarcoplasmic reticulum membrane (Block et al., 1988; Rios and Brum, 1987; Tanabe et al., 1987). Depolarization of the plasma membrane activates Ca_v1.1 which in turn activates RyR1, leading to massive Ca²⁺ release into the myoplasm of the cell. This Ca²⁺ interacts with proteins of the sarcomere, leading to muscle contraction. Despite decades of research, the exact nature of the link between Ca_v1.1 and RyR1 remains unknown.

Recently, STAC3 was identified as an essential component of the EC coupling machinery. Cells lacking STAC3 are unable to produce the Ca²⁺ transients definitive of EC coupling (Horstick et al., 2013; Nelson et al., 2013). STAC3 is one of only five proteins necessary to reconstitute EC coupling in non-muscle cells (Perni et al., 2017). It consists of an N-terminal C1 domain connected via an intrinsically disordered region to tandem SH3 domains (Wong King Yuen et al., 2017). Two other isoforms, STAC1 and STAC2, also exist and share high sequence identity with STAC3; they are expressed in a variety of tissues, including the brain.

STAC proteins form multiple functional interactions with Ca_v1 channels. Two independent studies showed that the STAC tan-

dem SH3 domains bind to the II-III loop of Ca_v1.1 (Polster et al., 2018; Wong King Yuen et al., 2017), a cytoplasmic linker in the channel long known to be essential for skeletal muscle EC coupling (Grabner et al., 1999; Nakai et al., 1998). Another proposed interaction is with a short peptide within the intrinsically disordered region of STACs, also known as the U-motif, and the proximal C terminus of Ca_v1 channels (Niu et al., 2018). In addition, the STAC C1 domain and the IQ domain of L-type calcium channels were also found to be required for stable interactions (Campiglio et al., 2018a; Campiglio and Flucher, 2017). In other L-type channels, STACs are able to abolish calcium-dependent inactivation (Campiglio et al., 2018a; Niu et al., 2018; Polster et al., 2015; Wong King Yuen et al., 2017) and voltage-dependent inactivation (Wong King Yuen et al., 2017).

STAC3 is the target for mutations causing the rare neuromuscular disease Native American myopathy (NAM). This disease was originally found to affect Native Americans of the Lumbee tribe in North Carolina but has also been reported in people of other descent. NAM causes debilitating symptoms such as muscle weakness, scoliosis, cleft palate, and susceptibility to malignant hyperthermia (MH) (Horstick et al., 2013; Linsley et al., 2017; Telegrafi et al., 2017; Zaharieva et al., 2018). It is estimated that one-third of patients die before the age of 18 years. Susceptibility to MH is mostly associated with mutations in RyR1, the skeletal muscle ryanodine receptor (Fujii et al., 1991; Pancaroglu and Van Petegem, 2018), suggesting that STAC3 may also interact with RyR1, as proposed by colocalization studies (Campiglio et al., 2018b). However, thus far no precise contacts have been



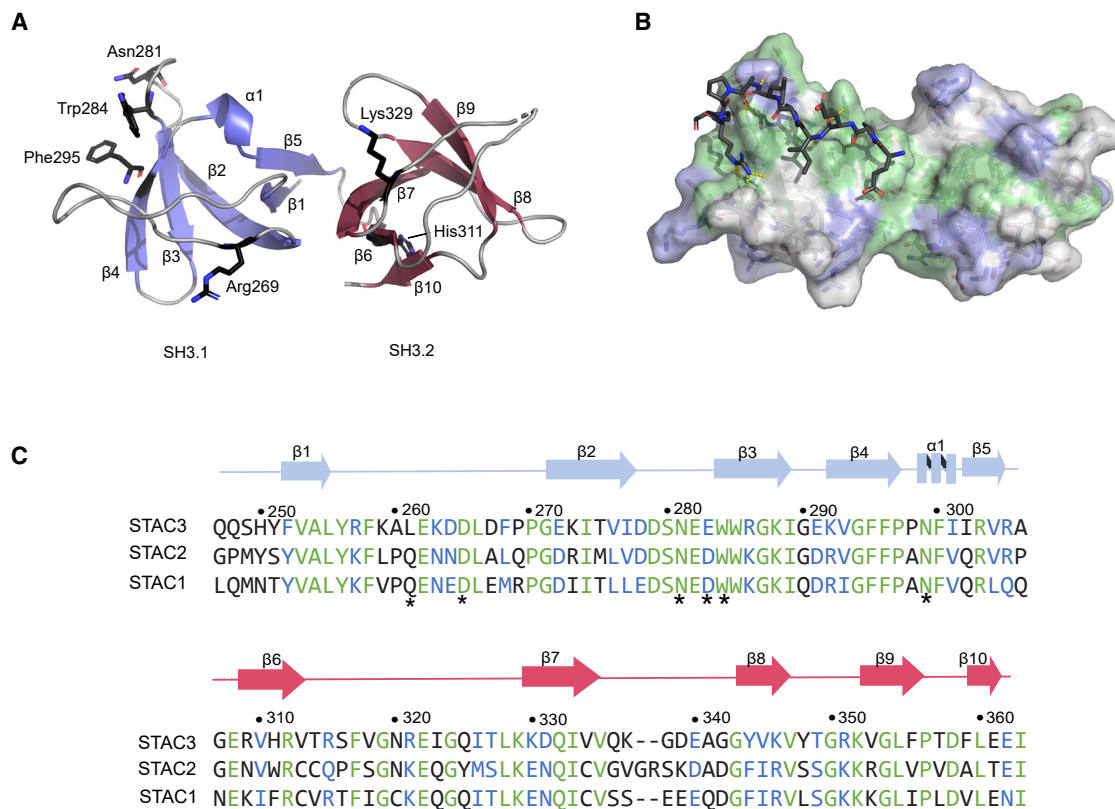


Figure 1. The STAC Isoforms Have High Sequence and Structural Similarity

(A) Cartoon representation of the human STAC3 tandem SH3 domains. β strands and an α helix are labeled. NAM-associated variants are highlighted in black, as well as the position for Arg269, which was introduced to stabilize the protein.

(B) Surface representation of human STAC3 aligned with the Cav1.1 II-III loop (PDB: 6B27). Human STAC3 is colored according to conservation with human STAC1 and human STAC2. Green, completely conserved; blue, residue property conserved; white, not conserved. Nearly all direct interactions the II-III loop make with STAC2 are through conserved residues.

(C) Sequence alignment of the three human STAC isoforms, with numbering of STAC3 indicated. Green highlights completely conserved residues, blue highlights property conservation. Residues marked with the * symbol indicate direct interaction with the Ca_v1.1 II-III loop (based on PDB: 6B27). Accession numbers are STAC1, UniProt: Q99469; STAC2, UniProt: Q6ZMT1; STAC3, UniProt: Q96MF2. See also Figure S1.

described. The role of this protein in a congenital myopathy highlights its importance in EC coupling and necessitates further research of its function in skeletal muscle.

As multiple sequence variants for STAC3, found in patients with myopathy, are reported in the ClinVar database (www.clinvar.com), we aimed to investigate their effect on structure and function. We report crystal structures of the tandem SH3 domains of STAC3 and characterize the effect of several sequence variants via X-ray crystallography, their effect on stability and ability to bind the Ca_v1.1 II-III loop, and on EC coupling.

RESULTS

Crystal Structure of a Stabilized Human STAC3 Tandem SH3 Domain Construct

Previously, we reported the structures of the STAC1 and STAC2 tandem SH3 domains (Wong King Yuen et al., 2017) but were unable to crystallize the tandem SH3 domains of STAC3. Whereas the purified STAC3 tandem SH3 domains readily precipitated upon concentration, the STAC1 and STAC2 counterparts never showed this issue. We thus compared the sequences to ratio-

nalize this difference. Based on this analysis, we mutated a surface-exposed proline (Pro269) in a loop of the first SH3 domain to an arginine, thus mimicking the equivalent Arg in STAC1. Whereas wild-type STAC3 would readily precipitate at concentrations above 70 μ M, the P269R mutant could readily be concentrated to 10-fold higher. Importantly, the mutation is not in a position where it is expected to affect binding to the II-III loop and has no effect on EC coupling as described later.

For simplicity, we refer to the human STAC3 P269R mutant as STAC3*, as all further variants in this manuscript were generated in the background of this stabilizing mutation. We solved a crystal structure of the STAC3* tandem SH3 domains to 2.1 \AA resolution (Figure 1A). Similar to the other STAC isoforms, each domain consists of a five-stranded antiparallel β sheet with the two domains connected by a short five-residue linker (Figure S1). Attempts to co-crystallize STAC3* in complex with the Cav1.1 II-III loop were unfruitful.

Sequence alignment of the STAC isoforms (Figure 1C) shows that most residues directly interacting with the Ca_v1.1 II-III loop (II-III loop) from the STAC2-Ca_v complex (PDB: 6B27) are conserved in all three isoforms, with a few exceptions (Figures

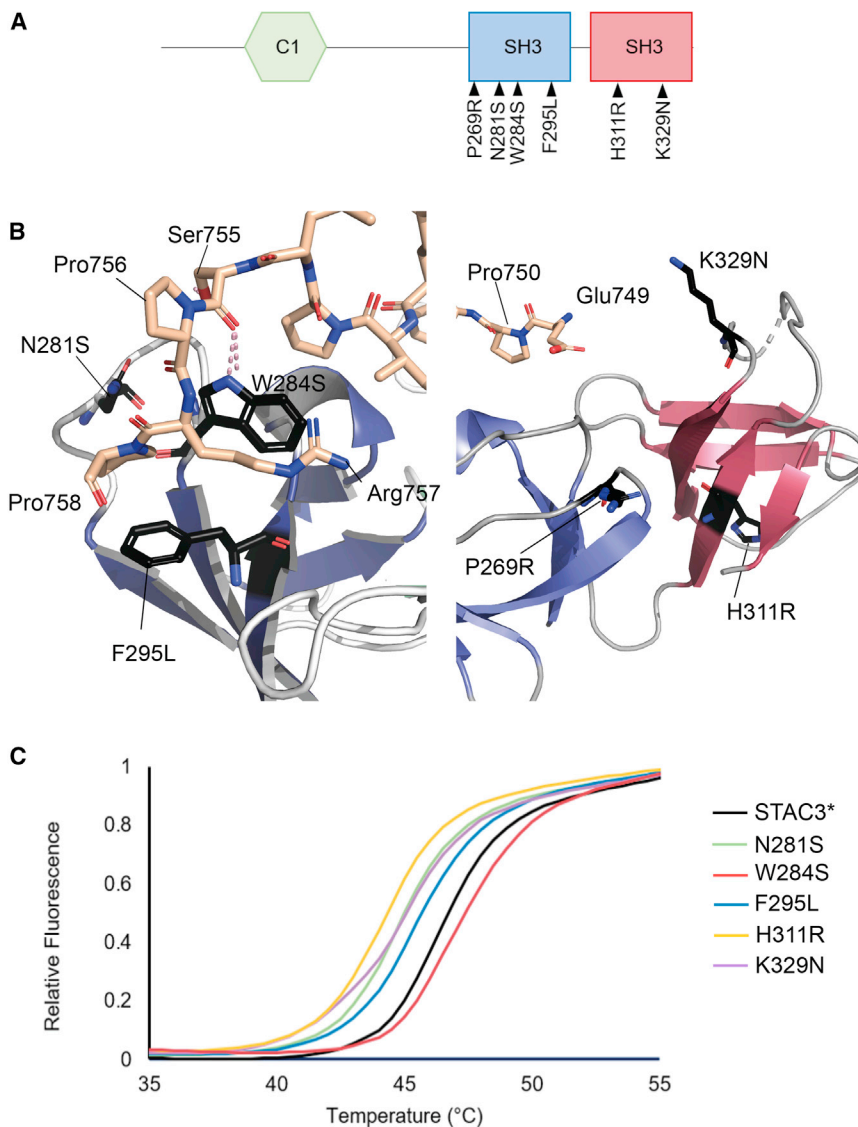


Figure 2. Mutations in the Tandem SH3 Domains of STAC3 Are Associated with Native American Myopathy

(A) Domain architecture of STAC3. It consists of a C1 domain, intrinsically disordered regions, and tandem SH3 domains. Sequence variants, as well as the stabilizing P269R mutation, are indicated by arrows.

(B) Location of NAM variants and the stabilizing P269R mutation within the STAC3 SH3 domains. Variants are highlighted in black, and the Ca_v1.1 II-III loop from PDB: 6B27 is aligned and shown in beige.

(C) Thermal melts of the STAC3* tandem SH3 variants. T_{1/2} values are shown in Table S1. See also Figure S3 and Table S2.

cause disease. Figure 2 shows the locations of five variants on the STAC3 tandem SH3 structure, with the Ca_v1.1 II-III loop peptide aligned to the structure for reference. All three variants in the first SH3 domain are in proximity to the peptide and thus are predicted to affect the binding. In contrast, neither of the two variants in the second SH3 domain is contacting the peptide directly, but we previously postulated that the SH3-2 domain may contribute to binding via delocalized electrostatic interactions (Wong King Yuen et al., 2017).

Effect of STAC3 Variants on Thermal Stability

Since disease mutations may affect the folding of the protein, which would provide a trivial explanation for their ability to cause disease, we assessed the thermal stability of the five variants via thermal melt assays (Figure 2C). All variants are prepared on the background STAC3*, so any change induced by these variants

1B, 1C, and S2). STAC2 residue Gln306, which makes hydrogen bond interactions with Arg757 of the II-III loop, is replaced by Leu261 in STAC3, so would lead to a net loss of a hydrogen bond. In addition, STAC2 residue Asp328, which hydrogen bonds to Ser755 of the II-III loop, is replaced by Glu283 in STAC3 (Figure S2). It is unclear whether this residue could substitute for the hydrogen bond with Ser755. Superposition of STAC2 and STAC3 yields a root-mean-square deviation (RMSD) of 0.84 Å over 113 C α atoms, highlighting the structural conservation.

STAC3 is the target for mutations causing NAM. The most commonly reported mutation is a tryptophan to serine substitution at position 284 in the first SH3 domain, which has been established as causative (Table S2) (Horstick et al., 2013). The equivalent residue in STAC2 forms several key interactions with the II-III loop. There have been several other STAC3 variants residing in the tandem SH3 domains reported in the ClinVar database (www.clinvar.com). Although they have been found in patients with myopathy, it remains to be proven that these truly

should be seen as relative. All variants mildly destabilized the protein, with the exception of W284S, which slightly increased stability (Table S1). The largest change in stability was for H311R, which had a T_{1/2} 1.6°C less than STAC3*. Such changes are minor compared with mutations previously analyzed for domains in RyRs or voltage-gated sodium channels, where often destabilizing shifts larger than 10°C have been reported (Gardill et al., 2018; Yuchi et al., 2012). Thus, these variants are unlikely to affect STAC3 function through a destabilization of the protein fold.

A novel mutation was discovered in a patient of Turkish descent, which causes aberrant splicing resulting in a four-residue (333–336) deletion in the SH3-2 domain of STAC3 (Grzybowski et al., 2017). These residues are located at the interface of the two SH3 domains and would affect an entire β strand, which is predicted to cause misfolding of the SH3-2 domain. This mutant expressed well as a fusion to maltose-binding protein but aggregated upon removal of this tag. Figure S3 displays a size exclusion chromatogram of the deletion mutant, showing a high

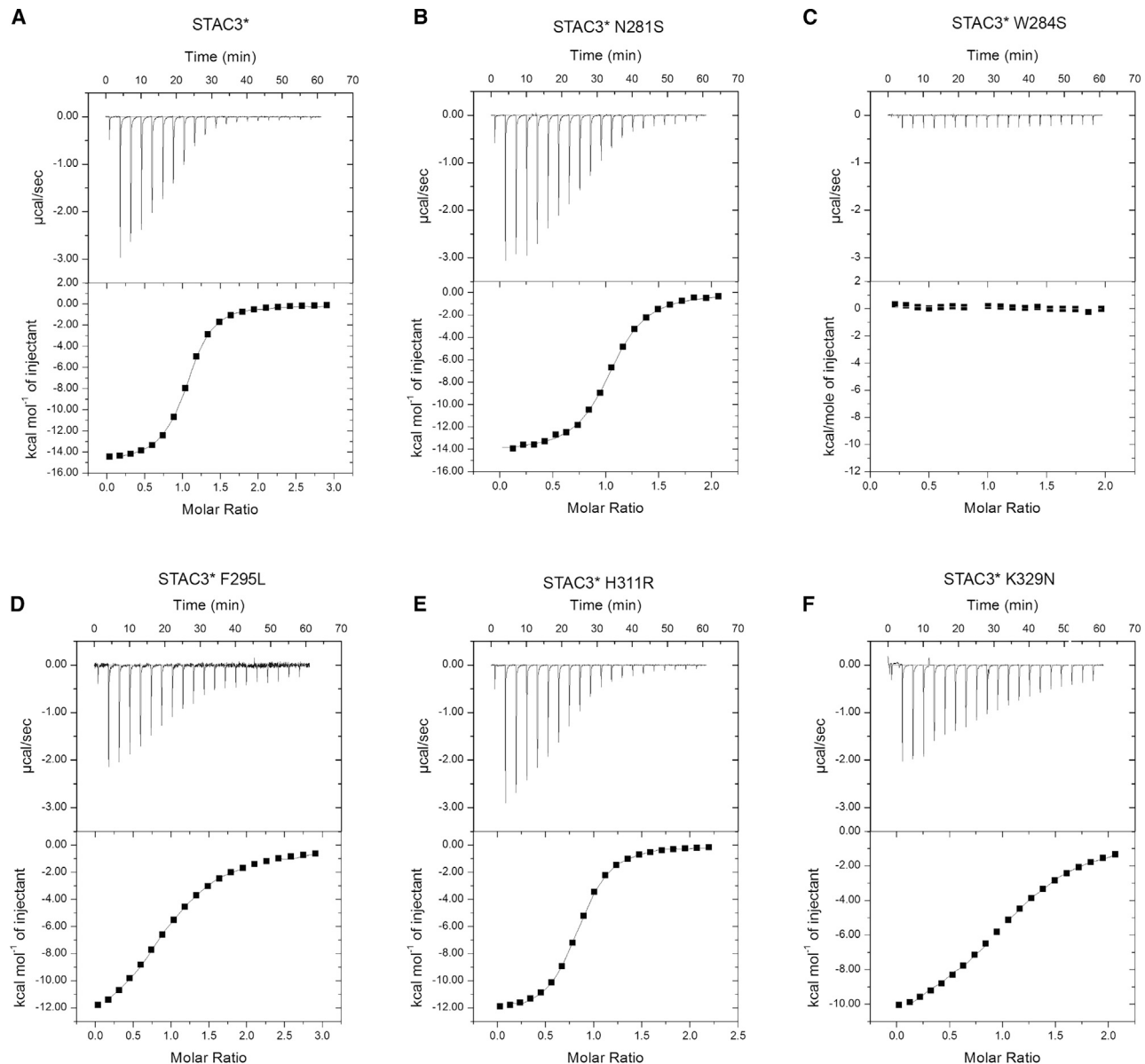


Figure 3. ITC Experiments Reveal the Effects of Native American Myopathy Mutations on Binding of Human STAC3* to the $Ca_v1.1$ II-III loop 1 mM $Ca_v1.1$ II-III loop (residues 728–775) titrated into 100 μ M STAC3* tandem SH3 domains (residues 245–364) with each variant: (A) STAC3*; (B) STAC3* N281S; (C) STAC3* W284S; (D) STAC3* F295L; (E) STAC3* H311R; (F) STAC3* K329N. See also [Table S4](#).

degree of aggregation. We postulate that this aggregation, likely due to misfolding of the SH3-2 domain, is responsible for the disease phenotype.

Effect of STAC3 Variants on Binding to the $Ca_v1.1$ II-III Loop

The STAC SH3 domains form a binding site for the $Ca_v1.1$ II-III loop, and disruption of this interaction strongly perturbs EC coupling (Polster et al., 2018; Wong King Yuen et al., 2017). We hypothesized that some of the proposed STAC3 disease variants may weaken this interaction, thereby leading to defective EC coupling in patients. To test this hypothesis, we performed isothermal titration calorimetry (ITC) experiments where we

titrated a human $Ca_v1.1$ II-III loop peptide (residues 728–775) into the human STAC3* tandem SH3 domains containing the disease-associated variants (Figures 3A–3F, Table S4). Binding of STAC3* yields a K_d of $\sim 2\mu$ M (Table 1).

Residue Asn281 is located in the first SH3 domain, proximal to the II-III loop (Figure 2B). The N281S mutant did not show any significant change in the interaction affinity (Figure 3, Table 1). In contrast, F295L reduced the K_d by 8-fold. The Phe295 residue is located in the first SH3 domain and makes van der Waals interactions with Pro758 in the II-III loop.

We did not detect binding between the II-III loop and the W284S mutant. This tryptophan is central to the interaction with the II-III loop; the side chain nitrogen hydrogen bonds the

Table 1. Thermodynamic Parameters Obtained from ITC Analysis of the Indicated Variants on STAC3*

Mutant	K_d (μ M)	ΔH (kcal/mol)	ΔS (cal/mol/K)	N value	Repeats
STAC3*	2.0 ± 0.2	-15.3 ± 0.4	-25.4 ± 2	0.92 ± 0.09	3
N281S	3.1 ± 0.4	-13.5 ± 0.9	-20.2 ± 3	1.05 ± 0.04	2
W284S	no binding determinable				
F295L	16.0 ± 1	-14.8 ± 0.3	-27.7 ± 1	1.15 ± 0.2	3
H311R	3.3 ± 0.3	-12.0 ± 0.1	-15.2 ± 3	0.88 ± 0.07	3
K329N	18.4 ± 0.3	-11.9 ± 0.1	-18.1 ± 0.4	1.0 ± 0.2	2

Errors indicated are standard deviations.

main chain of the peptide, and it forms cation-pi interactions with Arg757 of the loop. Elimination of these interactions thus strongly perturbs binding to a level where it is no longer detectable via ITC.

The second SH3 domain contributes less strongly to binding than the first (Wong King Yuen et al., 2017). We observed no reduction in binding affinity for the H311R mutant, located in the second SH3 domain. However, K329N, a surface-exposed residue in the second SH3 domain reduced the binding affinity by 9.2-fold.

Structural Impact of the W284S and K329N Variants

Because of the large impact of W284S on binding, we wanted to test whether this variant could result in conformational changes.

We solved a 1.6 Å crystal structure of the W284S STAC3* tandem SH3 domains (Figures 4A and 4B, Table 2). A superposition with STAC3* shows that the overall fold of the protein is maintained, yielding an RMSD of 0.63 Å over 106 C α atoms. Only minor changes in side-chain conformations near residue 284 can be seen. However, there is no overall misfolding, indicating that the major effect of this mutation is elimination of the key interactions with the II-III loop.

The K329N variant is located in the SH3-2 domain, and the corresponding residue in STAC2 was not observed to interact directly with the Ca v 1.1 II-III loop peptide in a crystal structure of the complex (Wong King Yuen et al., 2017). However, the variant does affect binding affinity \sim 9-fold, so we wondered whether it could have an allosteric effect. We therefore solved a 1.7 Å crystal structure of this mutant in the context of the STAC3* tandem SH3 domains (Figures 4A and 4C, Table 2). The structure superposes well with STAC3*, with an RMSD of 0.98 Å over 107 C α atoms. Importantly, no major changes were observed in the binding site for the II-III loop, begging the question of how the K329N mutant reduces the affinity 9-fold. Previously, we found that SH3-2 domain in STAC2 contributes to the binding affinity for the Ca v 1.1 II-III loop (Wong King Yuen et al., 2017). In the crystal structure of the STAC2 tandem SH3 domains in complex with the II-III loop peptide, we found that Glu749 in the II-III loop forms a water-mediated hydrogen bond with Lys374 in the SH3-2 domain. The equivalent residue in STAC3 is Lys329, so we attribute the loss in affinity, at least in

Table 2. X-Ray Data Collection and Refinement Statistics

	STAC3* Tandem SH3	STAC3* Tandem SH3 W284S	STAC3* Tandem SH3 K329N
Space group	P6 $_2$	C 1 2 1	P3 $_2$
Cell dimensions			
a, b, c (Å)	87.805, 87.805, 28.835	84.032, 29.331, 57.143	87.878, 87.878, 29.452
α , β , γ (°)	90, 90, 120	90, 129.622, 90	90, 90, 120
Resolution (Å)	38.02–2.105 (2.18–2.105)	41.68–1.6 (1.657–1.6)	28.76–1.649 (1.708–1.649)
R $_{pim}$	0.012 (0.209)	0.046 (0.158)	0.028 (0.355)
I/ σ	60.2 (4.3)	23.3 (4.95)	27.3 (1.8)
Completeness	96.65 (80.19)	88.59 (53.51)	95.83 (98.55)
Redundancy	6.0 (4.5)	2.6 (2.0)	4.8 (3.3)
No. of reflections	7,349 (593)	12,785 (762)	29,433 (2,993)
R $_{work}$ /R $_{free}$	0.2214/0.2733	0.1826/0.2068	0.1966/0.2060
No. of atoms			
Protein	843	970	1845
Ligand	8	9	21
Water	41	141	216
B factors			
Protein	38.03	16.71	25.03
Ligand	25.69	27.24	25.57
Water	35.46	27.68	38.59
Ramachandran favored (%)	98.13	99.17	98.29
Ramachandran allowed (%)	1.87	0.83	1.71
Ramachandran outliers (%)	0	0	0
Root-mean-square deviation			
Bond lengths (Å)	0.01	0.005	0.022
Bond angles (°)	0.90	0.66	1.87

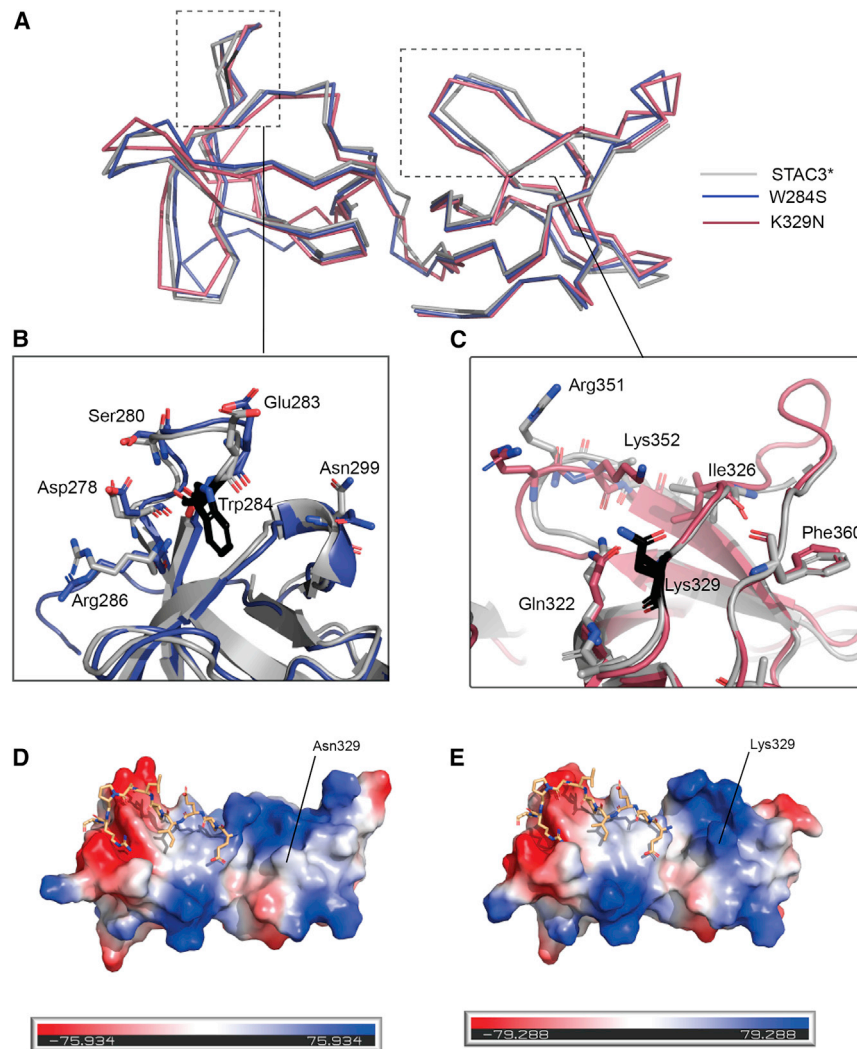


Figure 4. Comparison of Human STAC3* Variant Structures with STAC3*

(A) Superposition of human STAC3* with K329N and W284S.

(B) Superposition of STAC3* with W284S in the region highlighted by the dashed box. Trp284 is represented in black. Side chains with the largest conformational changes are shown as sticks.

(C) Superposition of STAC3* with K329N in the region highlighted by the dashed box. Lys329 is represented in black. Side chains with the largest conformational changes are shown as sticks.

(D) Electrostatic surface potential of the STAC3*K329N mutant.

(E) Electrostatic surface potential for STAC3*. The range for coloring is indicated below in $k_B T e_c^{-1}$, where k_B is the Boltzmann constant, T is the absolute temperature in Kelvin, and e_c is the absolute value of the charge of a proton.

See also [Table S4](#).

course of the simulations ([Figures S4A and S4B](#)). The water-mediated hydrogen bond between Ca_v1.1 Glu749 and STAC2 Lys374, observed in our previously reported crystal structure (PDB: 6B27), is also formed transiently during the MD simulation of the STAC2: Ca_v1.1 peptide complex, as is the equivalent water-mediated hydrogen bond involving STAC3* Lys329 ([Figure 5A](#)). In addition, a transient direct salt bridge is observed between Ca_v1.1 Glu749 and STAC2 Lys374 or STAC3* Lys329 ([Figure 5B](#)). These results thus help explain the impact of the K329N mutation, which reduces affinity for the Ca_v1.1 II-III loop peptide \sim 9-fold.

part, through the loss of this water-mediated hydrogen bond. In addition, there are three negatively charged residues in the Ca_v1.1 II-III loop peptide that were not visible in the STAC2 complex, likely because of flexibility. These may interact with positive charges in the SH3-2 domain. [Figure 4D](#) shows the electrostatic surface potential of the STAC3* tandem SH3 domains, showing a cluster of positive charges. This cluster is smaller in the K329N mutant ([Figure 4E](#)), which may also contribute to the lowered affinity.

Molecular Dynamics Simulations of STAC2 and STAC3* Bound to the Ca_v1.1 II-III Loop Peptide

In order to further probe the possible interactions of the Ca_v1.1 II-III loop peptide with the SH3-2 domain, we carried out microsecond molecular dynamics (MD) simulations of STAC2 in complex with the Ca_v1.1 II-III loop peptide, as well as STAC3* with the docked peptide ([Figure 5 and S4](#)). Throughout the 2 μ s simulations, the binding interactions between the Ca_v1.1 peptide and STAC3* are very similar to the STAC2:peptide interactions. For example, a salt bridge is observed between Ca_v1.1 residue Arg757 and STAC2 Asp310 or STAC3* Asp 265 throughout the

The MD simulation results are also consistent with the ITC data for the other STAC3* variants tested ([Figure 5C](#)). STAC3* Trp284 forms a hydrogen bond with Ca_v1.1 Ser755 throughout the MD simulation. The equivalent hydrogen bond, which we previously observed in the crystal structure of the STAC2: Ca_v1.1 peptide complex (PDB: 6B27), is also seen throughout the STAC2 complex simulation. Moreover, Phe295 in STAC3* is involved in transient cation- π interactions with Ca_v1.1 Arg757. This is consistent with the ITC data, which show a reduction in binding affinity when Phe295 is mutated to Leu. In contrast, Asn281 in STAC3* does not significantly interact with the Ca_v1.1 peptide, consistent with the mutation at this position not changing the binding affinity significantly. In summary, MD simulations highlight the similarities between STAC2 and STAC3* when in complex with the Ca_v1.1 II-III loop peptide and provide clear rationale for the ITC findings of the tested variants.

Generation of a Double Ca_v1.1/STAC3 KO Cell Line

To determine the effects of the analyzed STAC3 mutations on EC coupling, we inactivated the STAC3 gene in dysgenic

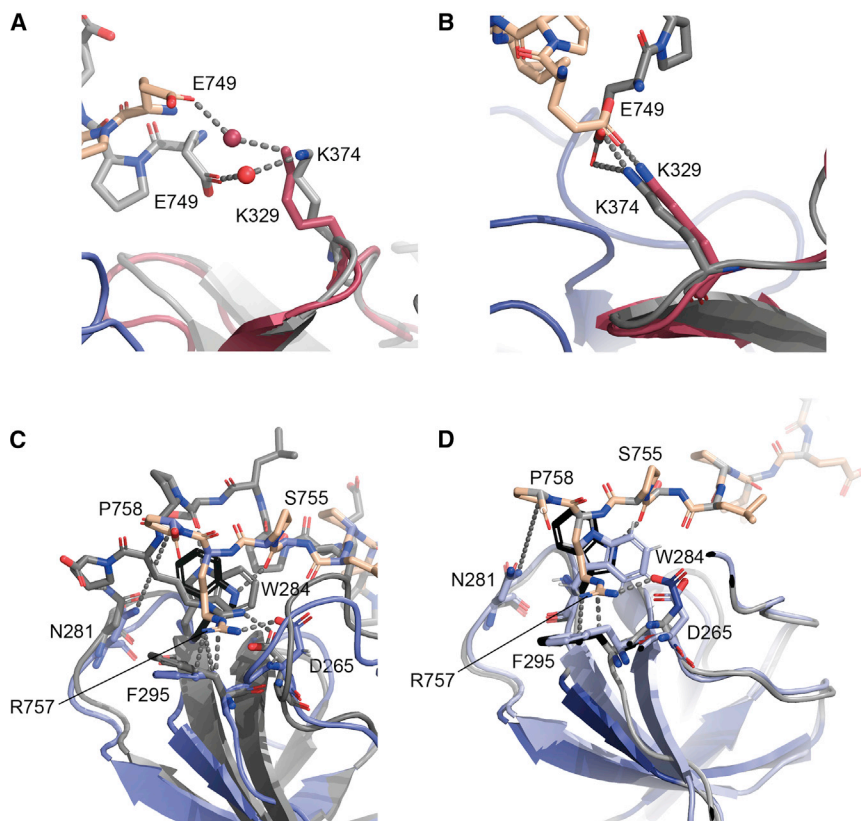


Figure 5. MD Simulations of the $Ca_v1.1$ Peptide in Complex with STAC2 and STAC3*

The STAC2 complex is shown in gray and the STAC3* complex in colors (blue, SH3-1 domain; red, SH3-2 domain; beige, $Ca_v1.1$ peptide).

(A) Representative MD structure with a water-mediated hydrogen bond between $Ca_v1.1$ Glu749 and STAC2 Lys374 or STAC3* Lys329. The water molecule is represented as a red sphere.

(B) Representative MD structures that show a direct salt bridge between $Ca_v1.1$ Glu749 and STAC2 Lys374 or STAC3* Lys329. The distances observed through the simulation are shown in Figure S4.

(C) Representative MD structures for the STAC2 and STAC3* complexes, showing several interactions (dashed lines).

(D) Overlay of the average structure from the STAC3* complex simulation (dark blue/black) and the experimentally derived STAC3 crystal structure (light blue) (PDB: 6UY7; this manuscript). See also Figure S4.

($Ca_v1.1^{-/-}$) mouse GLT cells through clustered regularly interspaced sort palindromic repeats (CRISPR)/Cas9-mediated mutagenesis. As a template for the mutagenesis, we selected a guide sequence that recognizes exon 6 of STAC3 and recruits Cas9 to introduce a double-strand break in the sequence coding for the linker region of STAC3 (Figure 6A). Early passage GLT cells were transfected with a vector encoding the guide sequence, Cas9, and GFP, which was used as a reporter for transfected cells. Forty-eight hours after the transfection, single GFP-positive cells were sorted into 96-well plates by flow cytometry. Individual cell clones were then propagated, differentiated, and examined for STAC3 expression levels in western blot analysis. Out of 30 clones, we selected clone F8 for use in experiments, based on its superior ability to differentiate into myotubes, its strong decrease in STAC3 mRNA transcription levels (Figure 6B), and lack of STAC3 protein expression (Figure 6C). Because a DNA template for homology-directed insertion was not introduced during the transfection, the genomic region was repaired through non-homologous end-joining, which causes insertion/deletion mutations. To determine the deletions and/or insertions in the F8 clone, we amplified the region of interest by PCR and inserted it into the pcDNA3 vector for sequencing, which confirmed the disruption of the coding sequence.

Genetic deletion of STAC3 in zebrafish and mouse was previously reported to suppress skeletal muscle EC coupling (Horstick et al., 2013; Linsley et al., 2017; Polster et al., 2016). We reconstituted the double $Ca_v1.1$ /STAC3 KO cell line (F8) with either GFP- $Ca_v1.1$ alone or with GFP- $Ca_v1.1$ in combination with

mouse STAC3 (mSTAC3) and analyzed depolarization-induced calcium transients. Reconstitution of only GFP- $Ca_v1.1$ failed to elicit calcium transients, both in response to single stimuli (Figure 6D) or to tetanic stimulation (Figure 6E), as expected in the absence of STAC3. To confirm that this lack of depolarization-induced calcium transients was a specific consequence of the loss of STAC3 rather than a non-specific effect of CRISPR/Cas9 mutagenesis, we reconstituted the F8 clone with both GFP- $Ca_v1.1$ and mSTAC3. This double reconstitution of F8 cells rescued robust calcium transients (Figures 6D and 6E), consistent with the notion that STAC3 is essential for skeletal muscle EC coupling.

Differential Effects of the Analyzed STAC3 Mutations on EC Coupling

To establish whether the reduced affinity for the II-III loop of $Ca_v1.1$ of some of the analyzed variants results in abolished or reduced EC coupling, we co-expressed the corresponding mSTAC3 variants in the F8 cell line together with GFP- $Ca_v1.1$ -N617D. The N617D mutation had been introduced in GFP- $Ca_v1.1$ to completely block calcium permeation through the L-type channel, without affecting its role in EC coupling (Dayal et al., 2017). Thus, possible contributions of Ca^{2+} influx to the depolarization-induced Ca^{2+} transients were excluded.

The numbering for the mutations in the mouse STAC3 differs from human STAC3. We confirmed that the P265R mutation (equivalent to human P269R), which we used to stabilize the human STAC3 tandem SH3 domains, had no effect on the Ca^{2+} transients (Figure S6).

Inserting the mouse N277S mutation (equivalent to human N281S) into mSTAC3 did not affect the mean peak amplitude of the Ca^{2+} transients (Figure 7, Table 3). This mutation also had the smallest effect on the affinity for the II-III loop (Table 1). The classic NAM mutation mouse W280S (human

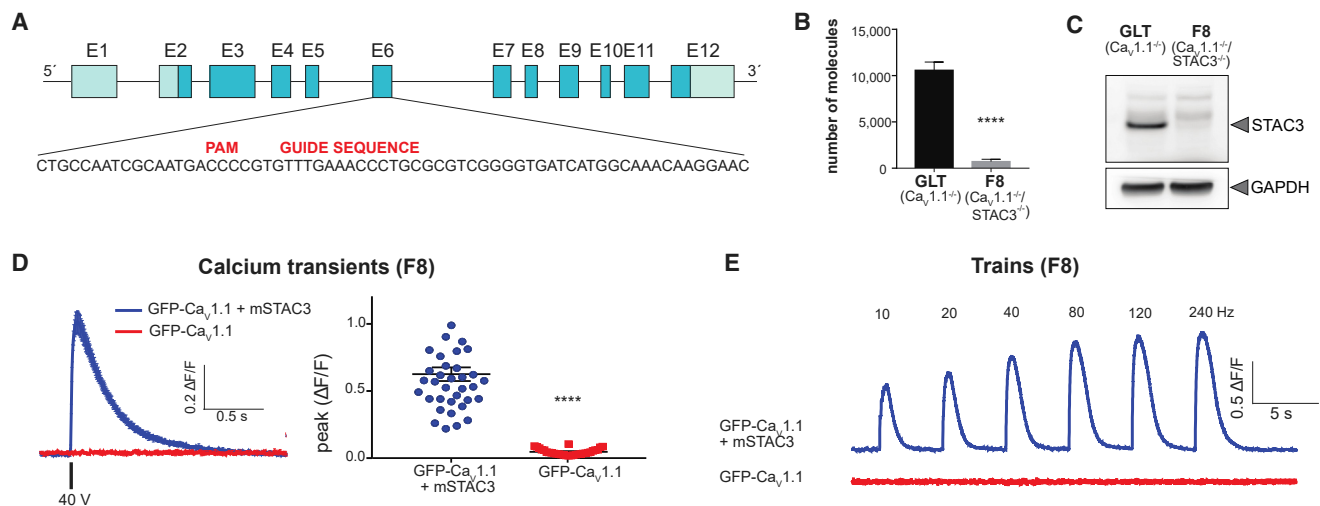


Figure 6. Generation and Characterization of a Double Ca_v1.1/STAC3 KO Cell Line (F8)

(A) Mouse *Stac3* (mSTAC3) locus with exons depicted. Exon 6 was mutagenized in GLT dysgenic (Ca_v1.1^{-/-}) cells after transfection with a vector containing the indicated guide sequence and Cas9.
 (B) mSTAC3 mRNA transcription levels in the F8 clone, assessed by TaqMan quantitative PCR, were greatly reduced compared with those of the dysgenic mother cell line (GLT). Mean values of three replicates.
 (C) Western blot analysis (one representative experiment of six is shown) with anti-STAC3 antibody indicated that the 50 kDa STAC3 band is expressed in the GLT cell line but lacking in the F8 cell line.
 (D) Average and peak values of calcium transients (ΔF/F) evoked by a single 2 ms 40 V field depolarization of F8 cells expressing GFP-Ca_v1.1 and mSTAC3 (blue) or only GFP-Ca_v1.1 (red).
 (E) Representative responses to tetanic stimulations of F8 myotubes with increasing frequencies. (N = 3 transfections; n_{GFP-Ca_v1.1} = 30; n_{GFP-Ca_v1.1+mSTAC3} = 37). Values are expressed as means ± SEM. ****p < 0.0001 (unpaired t test). See also Figure S6.

W284S) resulted in the largest reduction of the mean peak amplitude to 16% of the mSTAC3 control, in agreement with the most drastic effect on binding to the II-III loop. Mutations on mouse K325N (human K329N) and mouse F291L (human F295L) had the next largest effects, reducing the mean peak amplitude to 61% and 56%, respectively, again in agreement with their effect on binding. Generally, these results match well with the ITC experiments; those mutants which showed reduced binding to the II-III loop showed reduced EC coupling. However, mouse H307R (human H311R) did have a significant effect on the Ca²⁺ transients (reduction to 71%), despite having minimal impact on the affinity of II-III loop binding. Therefore, it is possible that this variant affects a critical interaction with another binding partner of STAC3, such as the RyR1.

DISCUSSION

STAC3 is an essential component of the skeletal muscle EC-coupling machinery. It can interact with a proline-rich region of the Ca_v1.1 II-III loop by virtue of tandem SH3 domains at its C terminus (Polster et al., 2018; Wong King Yuen et al., 2017). This interaction is essential for EC coupling, and the STAC3 W284S mutation, which affects a key residue in the interface, has been linked to NAM (Horstick et al., 2013).

We previously reported crystal structures of the tandem SH3 domains of human STAC1 and STAC2, as well as the SH3-2 domain of STAC3 (Wong King Yuen et al., 2017). However, attempts to crystallize the tandem SH3 domains of human STAC3 had failed due to precipitation of the protein at high con-

centrations. Here, we found that introduction of a stabilizing mutation, P269R, allows for crystallization, and ITC studies can be performed at higher protein concentrations. Importantly, the mutation is away from the II-III loop binding site and does not affect EC coupling. Although the affinities of the II-III loop peptide for STAC3 and STAC2 are very similar, a direct analysis of the STAC2:peptide crystal structure shows that a few residues are different in STAC3. However, MD simulations highlight the similarities between STAC2 and STAC3 in binding to Ca_v1.1.

As several new putative STAC3 disease variants have been reported in the ClinVar database, we aimed to investigate whether these may have an impact on binding of STAC3 to the II-III loop and affect EC coupling. We picked five variants in the tandem SH3 domains and introduced them in the background of STAC3* containing the stabilizing mutation. This allowed us to use higher concentrations of proteins, required for reliable ITC measurements and crystallization. We found that several variants affect both the affinity and EC coupling. The largest impact is obtained for the prototypical NAM mutation W284S, which is no surprise because this mutation affects a residue central in the interaction. Although we could no longer detect any binding via ITC, the variant does not completely abolish EC coupling, as many myotubes still respond with a small transient compared with the total loss of evoked calcium transients in the complete STAC3 knockout. This suggests there is still an interaction between STAC3-W284S and Ca_v1.1 in the native environment of a skeletal muscle cell, but so weak that it goes beyond the detection limit of ITC with the tandem SH3 domains and the isolated Ca_v1.1 II-III loop. An additional interaction has been proposed between the so-called U-motif in the STAC disordered linker

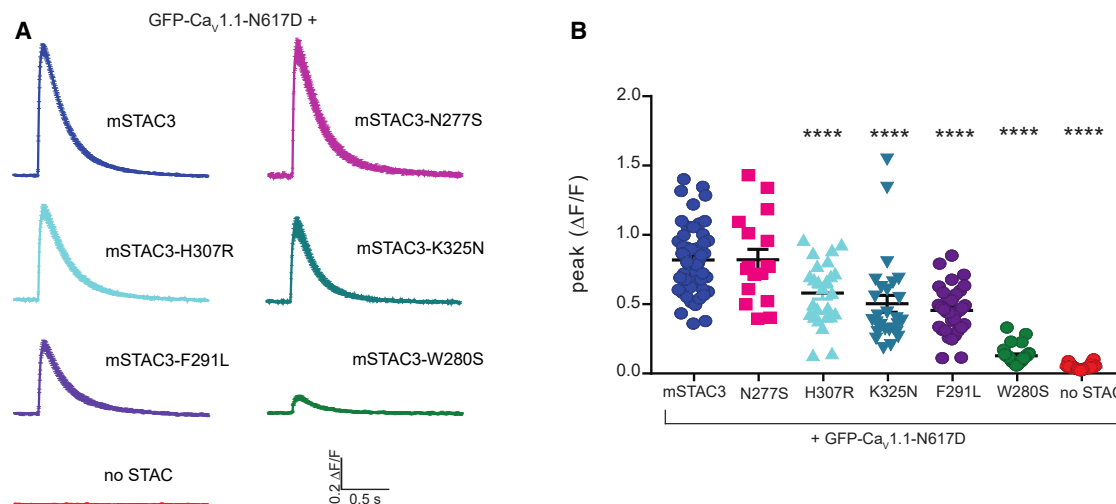


Figure 7. Effects of STAC3 Mutations on Depolarization-Induced Calcium Transients in Reconstituted Dysgenic/STAC3-Deficient (F8) Myotubes

(A) Representative calcium transients in response to single electrical pulses.

(B) Peak calcium transient amplitudes ($\Delta F/F$) evoked by a single 2 ms 40 V stimulus in F8 myotubes expressing GFP-Ca_v1.1-N617D and the indicated mSTAC3 mutant. (N = 5 transfections; $n_{\text{STAC3}} = 56$; $n_{\text{STAC3-N277S}} = 17$; $n_{\text{STAC3-H307R}} = 26$; $n_{\text{STAC3-K325N}} = 27$; $n_{\text{STAC3-F291L}} = 33$; $n_{\text{STAC3-W280S}} = 29$; $n_{\text{noSTAC3}} = 36$). Values are expressed as means \pm SEM. ANOVA $F_{(6,217)} = 71.47$; $p < 0.0001$; p values in the figure from Tukey post hoc analysis. **** $p < 0.0001$.

See also Table 3.

and the C-terminal region of the L-type Ca²⁺ channel (Niu et al., 2018), which may help promote the weak interactions with the W284S mutant. Of interest, the W284S substitution slightly increased the thermal stability. As the variant did not lead to any substantial structural changes, this may be due to the decreased exposure of a hydrophobic surface.

F295L affects a residue in the SH3-1 domain that directly interacts with the II-III loop. Decreasing the affinity \sim 8-fold, this mutation also causes a significant reduction in Ca²⁺ transients in EC-coupling assays. Interestingly, although all direct interactions with the Ca_v1.1 peptide are mediated by the SH3-1 domain, the K329N variant, located in the SH3-2 domain, resulted in a \sim 9-fold reduction in affinity and also affected EC coupling. This highlights the fact that both SH3 domains contribute to full binding affinity. Indeed, we previously found that the affinity of the II-III loop peptide for the STAC2 SH3-1 domain alone is \sim 40-fold weaker than for the tandem SH3 domains. The Lys374 residue in STAC2, equivalent to STAC3 Lys329, is involved in a water-mediated hydrogen bond with the II-III loop peptide, which likely contributes to the loss in affinity observed for K329N. This hydrogen bond is also detected in MD simulations for STAC3. In addition, the variant affects the electrostatic surface potential of the SH3-2 domain, which shows a cluster of positive charges in an area that could bind negatively charged residues in the II-III loop. Although these residues were not visible in the STAC2:II-III loop peptide structure, they may be interacting in a flexible fashion, resulting in uninterpretable electron density in the crystal structure. Indeed, during MD simulations, we found a transient direct salt bridge to form between STAC3* Lys329 and Ca_v1.1 Arg757. Although we did not see any significant effect of the substitution on the conformation, an additional possibility is that K329N affects the conformational dynamics of the SH3 domains.

Our study shows that multiple STAC3 disease variants can have an impact on binding to the Ca_v1.1 II-III loop and EC coupling, which may underlie myopathy. However, given that the effect is not as drastic as in the case of the classic NAM W284S mutation, the phenotype for such variants would be expected to be milder. Of the studied variants, the only detailed reports in the literature have been for W284S and Δ IVVQ (Grzybowski et al., 2017; Horstick et al., 2013; Stamm et al., 2008; Telegrafi et al., 2017; Waldrop et al., 2017; Zaharieva et al., 2018). The W284S mutation is found as homozygous or compound heterozygous with other loss-of-function mutations. Disease severity is variable among patients (Table S2). We performed a sequence comparison of STAC3 across >500 vertebrates (Figure S5 and Table S3) and found complete conservation for Trp284 and Asn281. Lys329 showed excellent conservation, whereas Phe295 and His311 were moderately conserved. However, for Phe295, it was only replaced by a Tyr residue, which should be able to compensate for the van der Waals and cation- π interactions with the II-III loop. Notably, Pro269, which was mutated to increase stability of STAC3, showed only moderate conservation.

Cryoelectron microscopy studies have revealed the structure of Ca_v1.1 at resolutions beyond 3 Å (Zhao et al., 2019). However, the II-III loop remains mostly unresolved, indicating a high intrinsic mobility. Thus, all structural insights into STAC3 binding are limited to the crystallographic studies. The II-III loop would be adjacent to the C-terminal region in three-dimensional space. The C-terminal domain, including the EF-hand and IQ domains, have been proposed as additional interaction sites for the STAC3 disordered linker and C1 domain, respectively. These seem sterically compatible with the SH3 binding to the II-III loop. Further studies with full-length Ca_v1.1 bound to STAC3 may shed more light on this.

Table 3. Parameters for the Ca²⁺ Transients Obtained for the Various Mouse STAC3 (mSTAC3) Variants

	GFP-Ca _v 1.1-N617D+							GFP-Ca _v 1.1		GFP-Ca _v 1.1-N617D+	
	mSTAC3	N277S	W280S	F291L	H307R	K325N	No STAC	mSTAC3	No STAC	mSTAC3	P265R
Peak (ΔF/F)	0.82 ± 0.03	0.82 ± 0.07	0.13 ± 0.01	0.46 ± 0.03	0.58 ± 0.04	0.50 ± 0.06	0.05 ± 0.00	0.63 ± 0.05	0.01 ± 0.00	1.36 ± 0.09	1.37 ± 0.11
Time to peak (ms)	62.8 ± 2.2	61.8 ± 4.0	85.9 ± 6.6	66.6 ± 3.4	63.4 ± 3.6	72.6 ± 3.8	–	–	–	52.2 ± 3.6	46.2 ± 13.7
Decay (ms)	265.3 ± 13.6	260.5 ± 22.5	283.5 ± 38.7	304.3 ± 29.6	280.8 ± 17.2	226.6 ± 19.5	–	–	–	262.0 ± 17.8	310.3 ± 24.6
n	56	17	29	33	26	27	36	37	30	19	22

Errors shown are standard errors of the mean. See also Figure S6.

STAR★METHODS

Detailed methods are provided in the online version of this paper and include the following:

- KEY RESOURCES TABLE
- RESOURCE AVAILABILITY
 - Lead Contact
 - Materials Availability
 - Data and Code Availability
- EXPERIMENTAL MODEL AND SUBJECT DETAILS
- METHOD DETAILS
 - Expression Constructs
 - Protein Expression and Purification
 - Crystallization and Structure Determination
 - Isothermal Titration Calorimetry
 - Thermal Melt Assay
 - Molecular Dynamics Simulations
 - CRISPR-Mediated Genome Editing in Dysgenic Cells
 - Cell Culture and Transfection
 - Expression Plasmids
 - RT-PCR
 - Western Blot
 - EC Coupling Analysis
- QUANTIFICATION AND STATISTICAL ANALYSIS

SUPPLEMENTAL INFORMATION

Supplemental Information can be found online at <https://doi.org/10.1016/j.str.2020.05.005>.

ACKNOWLEDGMENTS

We acknowledge the staff at the Stanford Synchrotron Radiation Lightsource beamline BL9-2 and the Advanced Photon Source beamline 23-ID-B, S. Sopper at the Innsbruck Flow Cytometry Unit, and I. Mahlknecht for excellent technical help in generating the F8 cell line. J.G. acknowledges funding from the Natural Sciences and Engineering Research Council of Canada (NSERC). F.V.P. acknowledges funding from the Canadian Institutes of Health Research (CIHR – PJT159601) and the RYR-1 Foundation. M.C. acknowledges funding from the Austrian Science Fund (FWF – T855) and (FWF – P30402) to B.E.F. B.R. acknowledges a fellowship from the Natural Sciences and Engineering Research Council of Canada (NSERC – CSG-M).

AUTHOR CONTRIBUTIONS

B.R., M.C., D.C., and J.M.B. performed the research. F.V.P., M.C., and B.E.F. designed and managed the project. B.R., M.C., and J.M.B. created the figures. The manuscript was written by B.R. and F.V.P. and edited by M.C. and B.E.F.

DECLARATION OF INTERESTS

The authors declare no competing interests.

Received: November 27, 2019

Revised: April 3, 2020

Accepted: May 11, 2020

Published: June 2, 2020

REFERENCES

- Adams, P.D., Afonine, P.V., Bunkoczi, G., Chen, V.B., Davis, I.W., Echols, N., Headd, J.J., Hung, L.W., Kapral, G.J., Grosse-Kunstleve, R.W., et al. (2010). PHENIX: a comprehensive Python-based system for macromolecular structure solution. *Acta Crystallogr. D Biol. Crystallogr.* **66**, 213–221.
- Andersen, H.C. (1980). Molecular dynamics simulations at constant pressure and/or temperature. *J. Chem. Phys.* **72**, 2384–2393.
- Block, B.A., Imagawa, T., Campbell, K.P., and Franzini-Armstrong, C. (1988). Structural evidence for direct interaction between the molecular components of the transverse tubule/sarcoplasmic reticulum junction in skeletal muscle. *J. Cell Biol.* **107**, 2587–2600.
- Bui, J.M., and Gsponer, J. (2014). Phosphorylation of an intrinsically disordered segment in Ets1 shifts conformational sampling toward binding-competent substates. *Structure* **22**, 1196–1203.
- Campiglio, M., Coste de Bagneaux, P., Ortner, N.J., Tuluc, P., Van Petegem, F., and Flucher, B.E. (2018a). STAC proteins associate to the IQ domain of CaV1.2 and inhibit calcium-dependent inactivation. *Proc. Natl. Acad. Sci. U S A* **115**, 1376–1381.
- Campiglio, M., and Flucher, B.E. (2017). STAC3 stably interacts through its C1 domain with CaV1.1 in skeletal muscle triads. *Sci. Rep.* **7**, 41003.
- Campiglio, M., Kaplan, M.M., and Flucher, B.E. (2018b). STAC3 incorporation into skeletal muscle triads occurs independent of the dihydropyridine receptor. *J. Cell. Physiol.* **233**, 9045–9051.
- Case, D.A., Ben-Shalom, I.Y., Brozell, S.R., Cerutti, D.S., Cheatham, T.E., III, Cruzeiro, V.W.D., Darden, T.A., Duke, R.E., Ghoreishi, D., Gilson, M.K., et al. (2018). AMBER 2018 (University of California, San Francisco).
- Darden, T., York, D., and Pedersen, L. (1993). Particle Mesh Ewald - an N.Log(N) method for Ewald Sums in large systems. *J. Chem. Phys.* **98**, 10089–10092.
- Dayal, A., Schrotter, K., Pan, Y., Fohr, K., Melzer, W., and Grabner, M. (2017). The Ca(2+) influx through the mammalian skeletal muscle dihydropyridine receptor is irrelevant for muscle performance. *Nat. Commun.* **8**, 475.

- Edelhoch, H. (1967). Spectroscopic determination of tryptophan and tyrosine in proteins. *Biochemistry* 6, 1948–1954.
- Emsley, P., Lohkamp, B., Scott, W.G., and Cowtan, K. (2010). Features and development of Coot. *Acta Crystallogr. D Biol. Crystallogr.* 66, 486–501.
- Fujii, J., Otsu, K., Zorzato, F., de Leon, S., Khanna, V.K., Weiler, J.E., O'Brien, P.J., and MacLennan, D.H. (1991). Identification of a mutation in porcine ryanodine receptor associated with malignant hyperthermia. *Science* 253, 448–451.
- Gardill, B.R., Rivera-Acevedo, R.E., Tung, C.C., Okon, M., McIntosh, L.P., and Van Petegem, F. (2018). The voltage-gated sodium channel EF-hands form an interaction with the III-IV linker that is disturbed by disease-causing mutations. *Sci. Rep.* 8, 4483.
- Grabner, M., Dirksen, R.T., and Beam, K.G. (1998). Tagging with green fluorescent protein reveals a distinct subcellular distribution of L-type and non-L-type Ca^{2+} channels expressed in dysgenic myotubes. *Proc. Natl. Acad. Sci. U S A* 95, 1903–1908.
- Grabner, M., Dirksen, R.T., Suda, N., and Beam, K.G. (1999). The II-III loop of the skeletal muscle dihydropyridine receptor is responsible for the Bi-directional coupling with the ryanodine receptor. *J. Biol. Chem.* 274, 21913–21919.
- Grzybowski, M., Schanzer, A., Pepler, A., Heller, C., Neubauer, B.A., and Hahn, A. (2017). Novel STAC3 mutations in the first non-American patient with native American myopathy. *Neuropediatrics* 48, 451–455.
- Horstick, E.J., Linsley, J.W., Dowling, J.J., Hauser, M.A., McDonald, K.K., Ashley-Koch, A., Saint-Amant, L., Satish, A., Cui, W.W., Zhou, W., et al. (2013). Stac3 is a component of the excitation-contraction coupling machinery and mutated in Native American myopathy. *Nat. Commun.* 4, 1952.
- Leaver-Fay, A., Tyka, M., Lewis, S.M., Lange, O.F., Thompson, J., Jacak, R., Kaufman, K., Renfrew, P.D., Smith, C.A., Sheffler, W., et al. (2011). ROSETTA3: an object-oriented software suite for the simulation and design of macromolecules. *Methods Enzymol.* 487, 545–574.
- Linsley, J.W., Hsu, I.U., Groom, L., Yarotsky, V., Lavorato, M., Horstick, E.J., Linsley, D., Wang, W., Franzini-Armstrong, C., Dirksen, R.T., et al. (2017). Congenital myopathy results from misregulation of a muscle Ca^{2+} channel by mutant Stac3. *Proc. Natl. Acad. Sci. U S A* 114, E228–E236.
- Lobo, P.A., and Van Petegem, F. (2009). Crystal structures of the N-terminal domains of cardiac and skeletal muscle ryanodine receptors: insights into disease mutations. *Structure* 17, 1505–1514.
- Maier, J.A., Martinez, C., Kasavajhala, K., Wickstrom, L., Hauser, K.E., and Simmerling, C. (2015). ff14SB: improving the accuracy of protein side chain and backbone parameters from ff99SB. *J. Chem. Theor. Comput.* 11, 3696–3713.
- McCoy, A.J., Grosse-Kunstleve, R.W., Adams, P.D., Winn, M.D., Storoni, L.C., and Read, R.J. (2007). Phaser crystallographic software. *J. Appl. Crystallogr.* 40, 658–674.
- Minor, W., Cymborowski, M., Otwinowski, Z., and Chruszcz, M. (2006). HKL-3000: the integration of data reduction and structure solution—from diffraction images to an initial model in minutes. *Acta Crystallogr. D Biol. Crystallogr.* 62, 859–866.
- Murshudov, G.N., Skubak, P., Lebedev, A.A., Pannu, N.S., Steiner, R.A., Nicholls, R.A., Winn, M.D., Long, F., and Vagin, A.A. (2011). REFMAC5 for the refinement of macromolecular crystal structures. *Acta Crystallogr. D Biol. Crystallogr.* 67, 355–367.
- Nakai, J., Tanabe, T., Konno, T., Adams, B., and Beam, K.G. (1998). Localization in the II-III loop of the dihydropyridine receptor of a sequence critical for excitation-contraction coupling. *J. Biol. Chem.* 273, 24983–24986.
- Nelson, B.R., Wu, F., Liu, Y., Anderson, D.M., McAnally, J., Lin, W., Cannon, S.C., Bassel-Duby, R., and Olson, E.N. (2013). Skeletal muscle-specific T-tubule protein STAC3 mediates voltage-induced Ca^{2+} release and contractility. *Proc. Natl. Acad. Sci. U S A* 110, 11881–11886.
- Niu, J., Dick, I.E., Yang, W., Bamgboye, M.A., Yue, D.T., Tomaselli, G., Inoue, T., and Ben-Johny, M. (2018). Allosteric regulators selectively prevent $Ca(2+)$ -feedback of CaV and NaV channels. *eLife* 7, e35222.
- Otwinowski, Z., and Minor, W. (1997). Processing of X-ray diffraction data collected in oscillation mode. *Methods Enzymol.* 276, 307–326.
- Pancaroglu, R., and Van Petegem, F. (2018). Calcium channelopathies: structural insights into disorders of the muscle excitation-contraction complex. *Annu. Rev. Genet.* 52, 373–396.
- Perni, S., Lavorato, M., and Beam, K.G. (2017). De novo reconstitution reveals the proteins required for skeletal muscle voltage-induced $Ca(2+)$ release. *Proc. Natl. Acad. Sci. U S A* 114, 13822–13827.
- Polster, A., Nelson, B.R., Olson, E.N., and Beam, K.G. (2016). Stac3 has a direct role in skeletal muscle-type excitation-contraction coupling that is disrupted by a myopathy-causing mutation. *Proc. Natl. Acad. Sci. U S A* 113, 10986–10991.
- Polster, A., Nelson, B.R., Papadopoulos, S., Olson, E.N., and Beam, K.G. (2018). Stac proteins associate with the critical domain for excitation-contraction coupling in the II-III loop of $CaV1.1$. *J. Gen. Physiol.* 150, 613–624.
- Polster, A., Perni, S., Bichraoui, H., and Beam, K.G. (2015). Stac adaptor proteins regulate trafficking and function of muscle and neuronal L-type Ca^{2+} channels. *Proc. Natl. Acad. Sci. U S A* 112, 602–606.
- Powell, J.A., Petherbridge, L., and Flucher, B.E. (1996). Formation of triads without the dihydropyridine receptor alpha subunits in cell lines from dysgenic skeletal muscle. *J. Cell Biol.* 134, 375–387.
- Rios, E., and Brum, G. (1987). Involvement of dihydropyridine receptors in excitation-contraction coupling in skeletal muscle. *Nature* 325, 717–720.
- Ryckaert, J.-P., Ciccotti, G., and Berendsen, H.J.C. (1977). Numerical-integration of cartesian equations of motion of a system with constraints - molecular dynamics of n-alkanes. *J. Comput. Phys.* 23, 327–341.
- Schlick, B., Flucher, B.E., and Obermair, G.J. (2010). Voltage-activated calcium channel expression profiles in mouse brain and cultured hippocampal neurons. *Neuroscience* 167, 786–798.
- Stamm, D.S., Aylsworth, A.S., Stajich, J.M., Kahler, S.G., Thorne, L.B., Speer, M.C., and Powell, C.M. (2008). Native American myopathy: congenital myopathy with cleft palate, skeletal anomalies, and susceptibility to malignant hyperthermia. *Am. J. Med. Genet. A* 146A, 1832–1841.
- Tanabe, T., Takeshima, H., Mikami, A., Flockerzi, V., Takahashi, H., Kangawa, K., Kojima, M., Matsuo, H., Hirose, T., and Numa, S. (1987). Primary structure of the receptor for calcium channel blockers from skeletal muscle. *Nature* 328, 313–318.
- Telegrafi, A., Webb, B.D., Robbins, S.M., Speck-Martins, C.E., FitzPatrick, D., Fleming, L., Redett, R., Dufke, A., Houge, G., van Harsseel, J.J.T., et al. (2017). Identification of STAC3 variants in non-Native American families with overlapping features of Carey-Fineman-Ziter syndrome and Moebius syndrome. *Am. J. Med. Genet. A* 173, 2763–2771.
- Vriend, G. (1990). WHAT IF: a molecular modeling and drug design program. *J. Mol. Graph.* 8, 52–56, 29.
- Waldrop, M.A., Boue, D.R., Sites, E., Flanigan, K.M., and Shell, R. (2017). Clinicopathologic conference: a newborn with hypotonia, cleft palate, micrognathia, and bilateral club feet. *Pediatr. Neurol.* 74, 11–14.
- Wong King Yuen, S.M., Campiglio, M., Tung, C.C., Flucher, B.E., and Van Petegem, F. (2017). Structural insights into binding of STAC proteins to voltage-gated calcium channels. *Proc. Natl. Acad. Sci. U S A* 114, E9520–E9528.
- Yuchi, Z., Lau, K., and Van Petegem, F. (2012). Disease mutations in the ryanodine receptor central region: crystal structures of a phosphorylation hot spot domain. *Structure* 20, 1201–1211.
- Zaharieva, I.T., Sarkozy, A., Munot, P., Manzur, A., O'Grady, G., Rendu, J., Malfatti, E., Amthor, H., Servais, L., Urtizberea, J.A., et al. (2018). STAC3 variants cause a congenital myopathy with distinctive dysmorphic features and malignant hyperthermia susceptibility. *Hum. Mutat.* 39, 1980–1994.
- Zhao, Y., Huang, G., Wu, J., Wu, Q., Gao, S., Yan, Z., Lei, J., and Yan, N. (2019). Molecular basis for ligand modulation of a mammalian voltage-gated $Ca(2+)$ channel. *Cell* 177, 1495–1506.e12.

STAR★METHODS

KEY RESOURCES TABLE

REAGENT or RESOURCE	SOURCE	IDENTIFIER
Antibodies		
Rabbit anti-STAC3	Proteintech	Cat#20392-1-AP; RRID: AB_10693618
Mouse anti-GAPDH	Santa Cruz Biotechnology	Cat#sc-32233; RRID: AB_627679
HRP-conjugated secondary antibody	Pierce	N/A
Bacterial and Virus Strains		
<i>Escherichia coli</i> Rosetta (DE3) pLacI	Novagen	Cat#70920
<i>Escherichia coli</i> NEB 5a	NEB	Cat#C29871
Chemicals, Peptides, and Recombinant Proteins		
SYPRO Orange Dye	Life Technologies	Cat#S6650
FugeneHD	Promega	Cat#E2311
Superscript II reverse transcriptase	Invitrogen	Cat#18064014
PMSF	Thermo Fisher	Cat#36978
Lysozyme	Biobasic	Cat#LDB0308
Deoxyribonuclease I from bovine pancreas	Sigma	Cat#11284932001
TCEP	Soltec Ventures	Cat#M115
DMEM	Gibco	Cat#31885-023
Fetal calf serum	Gibco	Cat#10500-064
Horse Serum	Gibco	Cat#16050-122
Fluo4-AM	Thermo Fisher	Cat#F14201
Critical Commercial Assays		
QuikChange site-directed mutagenesis	Agilent Technologies	Cat#200519
QIAprep Spin Miniprep Kit	Qiagen	Cat#27104
RNeasy Protect Mini Kit	Qiagen	Cat#74124
BCA assay	Thermo Scientific	Cat#23227
Quant-IT PicoGreen dsDNA Assay Kit	Invitrogen	Cat#P11496
QIAquick Gel extraction kit	Qiagen	Cat#28706
ECL Supersignal West Pico kit	Thermo Scientific	Cat#34577
Deposited Data		
STAC3 tandem SH3 – P269R Structure	This paper	PDB: 6UY7
STAC3 tandem SH3 – P269R, W284S Structure	This paper	PDB: 6UY9
STAC3 tandem SH3 – P269R, K329N Structure	This paper	PDB: 6UY8
Crystal structure of human STAC2 Tandem SH3 Domains (296-411)	(Wong King Yuen et al., 2017)	PDB: 6B26
Crystal structure of human STAC2 Tandem SH3 Domains (296-411) in complex with a CaV1.1 II-III loop peptide	(Wong King Yuen et al., 2017)	PDB: 6B27
Crystal structure of the second SH3 domain of STAC3 (309-364)	(Wong King Yuen et al., 2017)	PDB: 6B29
Experimental Models: Cell Lines		
Dysgenic cells (GLTs)	(Powell et al., 1996)	N/A
Dysgenic/STAC3 KO cell line F8	This paper	N/A
Oligonucleotides		
Refer to Table S5	This paper	N/A

(Continued on next page)

Continued

REAGENT or RESOURCE	SOURCE	IDENTIFIER
Recombinant DNA		
pX458 vector	Feng Zhang	Addgene #48138
Modified pET28 vector	Novagen	Addgene #69929
Software and Algorithms		
HKL2000	(Otwinowski and Minor, 1997)	http://www.hkl-xray.com/
Phaser	(McCoy et al., 2007)	http://ccp4.ac.uk
COOT	(Emsley et al., 2010)	https://www2.mrc-lmb.cam.ac.uk/personal/pemsley/coot/
Refmac5	(Murshudov et al., 2011)	http://ccp4.ac.uk
Origin	Malvern	N/A
CRISPR Design software	MIT	http://crispr.mit.edu
QuikChange Primer Design	Agilent	https://www.chem.agilent.com/store/primerDesignProgram.jsp
Phenix	(Adams et al., 2010)	https://www.phenix-online.org
PyMol	Schrödinger	https://pymol.org
Clampfit	Molecular Devices - Axon	https://mdc.custhelp.com
Prism	GraphPad Software Inc.	N/A
Other		
MicroAmp 48-well reaction plate	Applied Biosciences	Cat# 4375816
MicroAmp 48-well optical adhesive film	Applied Biosciences	Cat# 4375928
HisTrap	GE Healthcare	Cat#17524701
Poros MC Metal	Thermo Fisher	Cat# 1542906
Amylose Resin	New England Biolabs	Cat# E8021S
HiLoad 16/600 Superdex 200pg	GE Healthcare	Cat#28989335

RESOURCE AVAILABILITY**Lead Contact**

Further information and reagent requests should be addressed to lead contact Filip Van Petegem (filip.vanpetegem@gmail.com).

Materials Availability

The cell line generated in this study is available from M.C. for specified research purposes with a completed Material Transfer Agreement.

Data and Code Availability

The atomic coordinates and structure factors for STAC3 tandem SH3 domains (P269R) and the variants K329N and W284S have been deposited in the Protein Data Bank with accession codes PDB: 6UY7, 6UY8, 6UY9, respectively (<http://www.rcsb.org/>).

EXPERIMENTAL MODEL AND SUBJECT DETAILS

For crystallography and biochemical studies, *Escherichia coli* Rosetta (DE3) (Novagen) was used as source for materials. Cells were grown in 2xYT media at 37°C or 18°C for 20-24hrs.

The F8 double ($Ca_v1.1$ /STAC3) KO cell line was originated as described from the GLT dysgenic ($Ca_v1.1$) cell line (Powell et al., 1996).

METHOD DETAILS**Expression Constructs**

All constructs for ITC and X-ray crystallography (Table S4) were cloned into a modified pET28 vector (Novagen), containing a His6-tag, maltose-binding protein, and a cleavage site for the tobacco etch virus (TEV) protease. Mutations were introduced by site-directed mutagenesis. Briefly, the QuikChange Primer Design Program was used to design primers encoding the desired point mutation. The QuikChange Site-Directed Mutagenesis kit was used to amplify the human STAC3 tandem SH3 domains via PCR and the

product was digested with *DpnI* restriction enzyme. The DNA was transformed into *Escherichia coli* NEB5 α (New England Biolabs) and the plasmid was subsequently amplified using the QIAprep Spin Miniprep Kit (Qiagen).

Protein Expression and Purification

Proteins were expressed for 20–24 h in *Escherichia coli* Rosetta (DE3) pLacI (Novagen) grown in 2 \times YT medium at 18°C. Cells were lysed via sonication in 250 mM NaCl and 10 mM HEPES (pH 7.4) (Buffer A) supplemented with 1 mM PMSF, 25 μ g/mL DNaseI, 25 μ g/mL lysozyme, and 10% glycerol. Lysates were applied to HisTrap FF Crude columns (GE Healthcare), washed with 5 column volumes (CVs) of buffer A, and eluted with buffer B (containing 250 mM NaCl and 500 mM imidazole, pH 7.4). Following cleavage of both the STAC and Ca_v proteins with His-tagged TEV protease for 12–14 h at 4°C, dialyzing against buffer A, the proteins were applied to a HisTrap FF Crude column in buffer A and eluted with buffer B. The constructs were further purified by an Amylose column (New England Biolabs), washed with 2 CVs of buffer A supplemented with 50 mM CaCl₂, and eluted with buffer A plus 10 mM maltose. The collected flow-through fractions were concentrated by using 3-kDa MWCO Amicon concentrators before loading onto a Superdex200 16/600 or Superdex75 16/600 column (GE Healthcare) in buffer A.

Crystallization and Structure Determination

All crystallization was done on the human STAC3. The STAC3 tandem SH3 domains construct with the P269R stabilizing mutation was crystallized by using hanging-drop vapor diffusion at 4°C by mixing equal volumes of protein (10 mg/mL) and well solution, containing 0.1 M MES (pH 6.5), 6% (wt/vol) PEG8000, and 8% ethylene glycol. Crystals were soaked in a mixture of mother liquor and 25% ethylene glycol and flash-frozen. The tandem SH3 domain construct of STAC3-P269R/K329N was crystallized by hanging-drop vapor diffusion at 4°C and by mixing equal volumes of protein (8.6 mg/mL) and well solution, which contained 0.1 M MES (pH 6.5), 8% (wt/vol) PEG8000, and 8% ethylene glycol. Crystals were transferred to a cryosolution containing the mother liquor and 25% (vol/vol) ethylene glycol and flash-frozen. The tandem SH3 domain construct of STAC3-P269R/W284S was crystallized by hanging-drop vapor diffusion at 4°C by mixing equal volumes of protein (3.4 mg/mL) and well solution, which contained 0.1 M NaOAc (pH 5.5), 0.2 M Lithium sulfate, and 24% (wt/vol) PEG3350. Crystals were transferred to a cryosolution containing the mother liquor and 25% (vol/vol) ethylene glycol and flash-frozen. Diffraction data were collected at the Stanford Synchrotron Radiation Lightsource beamline BL9-2, and the Advanced Photon Source beamline 23-ID-B. Data sets were processed by using HKL2000 (Minor et al., 2006). The structure of all proteins was solved by molecular replacement via Phaser (McCoy et al., 2007), using the second SH3 domain of STAC3 (PDB ID 6B29) and the first SH3 domain of STAC2 (PDB ID 6B26) as search models. All models were completed with iterative cycles of manual model building in Coot (Emsley et al., 2010) and refinement with Refmac5 (Murshudov et al., 2011) or Phenix (Adams et al., 2010). Data and refinement statistics are shown in Table 2. All structure files are available in the PDB with accession codes 6UY7, 6UY8, and 6UY9.

Isothermal Titration Calorimetry

All proteins were dialyzed against 200 mM NaCl, 10 mM HEPES (pH 7.4) at 4°C, then concentrated. Protein concentrations were determined by using a UV/Vis spectrophotometer (Beckman Coulter), with proteins diluted in Edelhoch buffer (Edelhoch, 1967). Titrations consisted of 20 injections of 2 μ L each. Experiments were performed at 25°C and a stirring speed of 750 rpm on an ITC200 Instrument (GE Healthcare). All data were processed using Origin (Version 7.0), and isotherms generated by following a point-by-point subtraction of a reference titration of ligand into buffer.

Thermal Melt Assay

All proteins were concentrated to 72.5 μ M (1 mg/mL) in Buffer A supplemented with 1 mM TCEP. Samples were combined with a 500-fold dilution of SYPRO orange dye (Life Technologies) and loaded into MicroAmp 48-well reaction plates with Optical adhesive covers (Applied Biosciences). Samples were run on a StepOne Real-Time PCR System (Thermo Fisher) from 25°C to 91°C, increasing at increments of 0.5°C and reading fluorescence after each increase. Two biological replicates per sample were run, each with six technical replicates. Melting temperatures were obtained from the first derivative maximum of the transitions (Lobo and Van Petegem, 2009).

Molecular Dynamics Simulations

Molecular Dynamics (MD) simulation of the Ca_v1.1 II-III loop peptide bound to the SH3 domains of STAC2 was performed using the previously reported crystal structure (PDB 6B27) with the associated water molecules part of the starting structure. The MD simulations of the Ca_v1.1 II-III loop peptide bound to the STAC3* SH3 domains began with the docking of the peptide to STAC3* (PDB 6UY7, this report), using Rosetta dock (Leaver-Fay et al., 2011) and PDB 6B27 as a template. A standard MD simulation protocol was used (Bui and Gsponer, 2014). Briefly, protonation states for all titratable residues were determined. The effective pKa for each titratable group was computed as described previously (Vriend, 1990) using the WHATIF pKa calculation package. MD simulations were carried out using the modified AMBER ff14SB force field (Maier et al., 2015). The simulations began with 5000 steps of steepest descent energy minimization and were followed by the reassignments of velocities from the Maxwell distribution at 300 K every 1 ps for 5000 ps, and by a final equilibration of the system for 2.0 ns. After equilibration, the MD trajectories were integrated using the GPU-accelerated pmemd engine in Amber18 (Case et al., 2018). The simulations were conducted using the isobaric-isothermal ensemble (Andersen, 1980) at 300 K and 1 atmosphere and using long-range non-bonded interactions with a 12 Å residue-based cutoff. Long-range electrostatic forces were

calculated using the particle-mesh Ewald sum (Darden et al., 1993). Bonds to hydrogen atoms were maintained with the SHAKE algorithm (Ryckaert et al., 1977) and an integration step size of two femtoseconds was used. A total of four microseconds of MD simulations for the Ca_v1.1 II-III loop peptide bound to the SH3 domains of STAC2 and STAC3 were obtained.

CRISPR-Mediated Genome Editing in Dysgenic Cells

The vector for the generation of CRISPR/Cas9-mediated loss-of-function STAC3 cell lines was constructed using pX458 (a gift from Feng Zhang; Addgene Plasmid #48138). The oligonucleotide yielding a small guide RNA (sgRNA) targeting the exon 6 of STAC3 was designed using CRISPR Design software (<http://crispr.mit.edu>). Cloning was performed according to the Feng Zhang protocol available at https://media.addgene.org/cms/filer_public/95/12/951238bb-870a-42da-b2e8-5e38b37d4fe1/zhang_lab_grna_cloning_protocol.pdf. Briefly, complementary oligos containing the STAC3 guide RNA were annealed and inserted in pX458, after digestion with BbsI. Low-passage GLTs were plated on a 100 mm dish and transfected with 3.5 μg of pX458 vector with the STAC3 guide RNA using FugeneHD (Promega). Forty-eight hours after transfection, the cells were resuspended in ice cold PBS and single GFP-positive cells were sorted into 96-well plates containing growth medium using FACS Aria II flow cytometer (BD Biosciences). Negative control consisted of untransfected GLTs. Clones were selected based on their ability to differentiate into myotubes and the efficacy of reducing STAC3 expression levels as assessed in qRT-PCR and Western blot analysis.

Cell Culture and Transfection

Generation of the homozygous dysgenic (*mdg/mdg*) cell line GLT was previously described (Powell et al., 1996). No information is available on the gender of the mice used to generate the GLT cell line. As the F8 double knock out (Ca_v1.1/STAC3 KO) cell line is derived from the GLT cell line, no gender information is available for the F8 cell line as well. Muscle cells from both cell lines were cultured in growth medium (DMEM, 10% fetal calf serum, 10% horse serum) in plastic flasks for continued proliferation. For induction of fusion and differentiation of myoblasts into myotubes, the growth medium was changed to a serum-poor fusion medium (DMEM, 2% horse serum) two days after plating. Cells grown on carbon and gelatin coated coverslips (for calcium transients) or on plastic (for WB analysis and RT-PCR analysis) were transiently transfected with the plasmids of interest 4 days after plating using FuGeneHD transfection reagent (Promega), according to the manufacturer's instructions. A total of 0.5 μg of each plasmid DNA was used per 35 mm culture dish; for 60 mm dishes the amount was doubled; for 100 mm dishes 3.5 μg DNA were used.

Expression Plasmids

Mouse STAC3 mutations (N277S, F291L, H307R, K325N, P265R) were introduced into pc-STAC3 (Campiglio et al., 2018a) by splicing by overlap extension PCR. Briefly, the cDNA sequence of mouse STAC3 (nt 1–1080) was amplified in separate PCR reactions using pc-STAC3 as template with overlapping primers mutating the amino acid of interest. The two separate PCR products were then used as templates for a PCR reaction with flanking primers to connect the nucleotide sequences. The resulting fragment was then KpnI/XhoI digested and ligated into the corresponding sites of pc-STAC3.

The W280S mutation was introduced into pc-STAC3 by isolating the coding sequence from pc-STAC3-NAM-GFP (Campiglio and Flucher, 2017) by PCR with a reverse primer introducing a XhoI site. The PCR product was then digested and inserted in the corresponding sites of the pc vector, yielding pc-STAC3-W280S.

The non-conducting mutation N617D was introduced in GFP-Ca_v1.1 (Grabner et al., 1998) by splicing by overlap extension PCR. Briefly, the cDNA sequence of rabbit Ca_v1.1 (nt 890–2766) was amplified in separate PCR reactions using GFP-Ca_v1.1 as template with overlapping primers introducing the mutation A>1849>G. The two separate PCR products were then used as templates for a PCR reaction with flanking primers to connect the nucleotide sequences. The resulting fragment was then EcoRI/XhoI digested and ligated into the corresponding sites of GFP-Ca_v1.1, yielding GFP-Ca_v1.1-N617D.

Sequence integrity of the all newly generated constructs was confirmed by sequencing (MWG Biotech, Martinsried, Germany).

RT-PCR

RNA was isolated from DIV 9–10 of GLT and F8 cells using the RNeasy Protect Mini Kit (Qiagen). After reverse transcription (SuperScript II reverse transcriptase, Invitrogen), the absolute number of transcripts was assessed by quantitative TaqMan PCR (Mm01159196_m1, Thermo Fisher Scientific), using a standard curve generated from PCR products of known concentrations as described previously (Schlick et al., 2010). Briefly, a primer pair was designed to amplify the region corresponding to exons 6 and 7. The PCR product was extracted using the QIAquick Gel Extraction Kit (QIAGEN). Concentrations of PCR products were determined using Quant-IT PicoGreen dsDNA Assay Kit (Invitrogen). Standard curve dilution series ranging from 10¹ to 10⁷ DNA molecules were generated in water containing 1 μg/ml of poly-dC-DNA (Midland, TX, USA). qRTPCRs of the standard curve samples were performed in triplicates and samples without template (background) served as negative controls. In order to determine standard reliability the standard curves were repeated three times. Finally, average linear regressions were calculated for the combined results of all standard curve replicates.

Western Blot

Proteins isolated from CRISPR-treated GLT clones at DIV 9–10 were prepared as previously described (Campiglio and Flucher, 2017). Briefly, GLTs were trypsinized, centrifuged and lysed in RIPA buffer with a pestle and left on ice for 30 minutes. The lysates were then

centrifuged for 10 minutes and the protein concentration was determined using a BCA assay (Thermo Scientific). Protein extracts were then separated by SDS-PAGE (4-12%) at 196 V and 40 mA for 60 min and transferred to a PVDF membrane at 25 V and 100 mA for 3 h at 4°C with a semidry-blotting system (Roth). The blot was incubated with rabbit anti-STAC3 (1:2,000; Proteintech) and mouse anti-GAPDH (1:100,000; Santa Cruz Biotechnology) antibodies overnight at 4°C and then with HRP-conjugated secondary antibody (1:5000; Pierce) for 1 h at room temperature. The chemiluminescent signal was detected with ECL Supersignal West Pico kit (Thermo Scientific) and visualized with ImageQuant LAS 4000.

EC Coupling Analysis

Depolarization-induced calcium transients were recorded as previously described ([Wong King Yuen et al., 2017](#)). Briefly, DIV 9-10 double-reconstituted Ca_v1.1/STAC3 myotubes were loaded with 5 μM Fluo4-AM (Thermo Fisher) and 0.1% Pluronic F-127 in DMEM for 40 min at room temperature. The coverslips were then mounted in Tyrode solution (130 mM NaCl, 2.5 mM KCl, 2 mM CaCl₂, 2 mM MgCl₂, 10 mM HEPES, and 30 mM glucose). Calcium transients were elicited by passing 2-ms pulses of 40 V across the 19-mm incubation chamber at room temperature. Fluorescence signals from single myotubes were recorded with the PTI *Ratio-Master* microphotometry system (Horiba Scientific). Traces were normalized by calculating the $\Delta F/F$ ratio in Microsoft Excel, while time to peak and decay were analyzed in Clampfit. Data were analyzed with the one-way Anova or Student *t* test in GraphPad. Results are expressed as mean ± SEM, and graphs were assembled in GraphPad.

QUANTIFICATION AND STATISTICAL ANALYSIS

Where appropriate, statistical details are given in the [Method Details](#) section.